35th Annual International Conference of the IEEE EMBS
Osaka, Japan, 3 - 7 July, 2013

Sparse Bayesian Inference Methods for Decoding 3D Reach and Grasp Kinematics and Joint Angles with Primary Motor Cortical Ensembles

Zhe Chen, *Senior Member, IEEE*, Kazutaka Takahashi, *Member, IEEE*, and Nicholas G. Hatsopoulos

***Abstract*— Sparse Bayesian inference methods are applied to decode three-dimensional (3D) reach to grasp movement based on recordings of primary motor cortical (M1) ensembles from rhesus macaque. For three linear or nonlinear models tested, variational Bayes (VB) inference in combination with automatic relevance determination (ARD) is used for variable selection to avoid overfitting. The sparse Bayesian linear regression model achieved the overall best performance across objects and target locations. We assessed the sensitivity of M1 units in decoding and evaluated the proximal and distal representations of joint angles in population decoding. Our results suggest that the M1 ensembles recorded from the precentral gyrus area carry more proximal than distal information.**

***Index Terms*— Sparse Bayesian inference, neural decoding, primary motor cortex, reach-to-grasp movement**

I. Introduction

We reach and grasp a cup effortlessly, but reaching and grasping in unconstrained 3D space is a complex movement involving the coordination of the proximal arm and distal hand. Despite many efforts dedicated to studying how populations of neurons represent and encode a high-dimensional kinematic space (e.g., [1], [2]), a complete understanding of population codes of the primary motor cortex (M1) remains unclear. A decoding approach provides a way to gain further insight into neural codes [3]. Recently, several groups have tried to decode 3D reach to grasp movement using either spikes, multiunit activity, or local field potentials based on recordings in M1 and premotor (PMd and PMv) areas [4]–[9]. In this study, we apply three statistical models and sparse Bayesian inference methods to decode 3D reach and grasp kinematics with M1 neuronal ensembles. In addition, we systematically assess the sensitivity of M1 units in decoding different (proximal vs. distal) joints and their spatial contribution in M1 area.

II. Materials and Methods

A. Experimental Recordings and Data

Two primates (female rhesus macaques: monkeys O and A) were trained to reach and grasp objects with their right hand. Four objects with five hand configurations (key grip, D-ring horizontal, D-ring vertical, small D-ring and sphere) were presented at various target locations in the monkey's reaching space (Fig. 1). Each object was presented to the monkey in a block of at least 140 trials. The presentation order was pseudorandom so that the monkey could not predict the object location. Each trial consisted of four different periods: a premovement preriod; a movement period preceding the grasp; a hold period when the monkey held the object; and a release period when the robot retracted the object. The movement period lasted about 500–700 ms. Each monkey was chronically implanted with a 100-electrode microelectrode array in the arm-hand area of M1 in the left hemisphere, contralateral to the hand they used to grasp the objects. The array was placed parallel as close as possible to the central sulcus. During recording sessions, signals were amplified, filtered (0.3–7.5 kHz), and digitalized at 30 kHz. For each channel, a threshold was set above the noise band to sample a 1.6 ms duration of the signal waveform (48 samples). The signal waveforms were spike sorted off-line using a semiautomated MATLAB (MathWorks, Natick, MA) software developed in the Hatsopoulos laboratory.

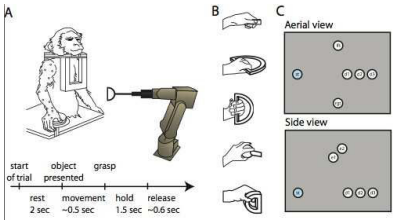

Fig. 1. An illustration of the 3D reach to grasp task for 5 objects (key grip, D-horizontal, D-vertical, sphere, small D-ring) at 7 locations (from [2]).

The 3D Cartesian positions of reflective markers placed on monkey's right forearm, wrist, hand, and fingers were recorded using an infrared based motion capture system (Vicon: Oxford Metrics, UK). The 3D velocities of wrist were computed based on the marker data directly. To compute the inverse kinematics (i.e., the joint angles from the marker positions), we used a scaled version of a skeletal model of the arm developed using the OpenSim platform (https://simtk.org/home/opensim). A total of 27 joint angles were computed for their angular positions and velocities. For the fingers, we modeled (i) flexion and extension at the carpal-metacarpal joint of the thumb, and at the metacarpo-phalangeal joints of the thumb/index/ring fingers, (ii) proximal interphalangeal joints of the thumb/index/ring fingers, and (iii) abduction and adduction of the thumb/index/ring fingers. For details of behavioral task, neural data acquisition and kinematics, the reader is referred to [2]. Here, we focus on the analysis on recordings from one monkey (O), in which $N_c = 44$ putative M1 units were collected in one recording session.

B. Neural Decoding: Sparse Bayesian Methods

1) Variable selection: For individual sorted units, we binned the spike trains into 40-ms bins and computed their smoothed firing rates. Upon preliminary correlation and regression analysis for optimal time lags between the kinematics and the spiking, we chose $[-160, 240]$ ms (negative/positive lag: before/after relative to the kinematics) as the optimal range. For a total of N_c units, we obtained a population firing rate vector with dimensionality of $10 \times N_c = 440$. We have included all units in the encoding/decoding analysis.

Given the large number of the input variables, it is important to choose statistical inference methods to avoid data overfitting. In order to use the recorded data more efficiently, instead of

Supported by NIH-NINDS Grant RO1-NS045853 (to N.G.H.) and an Early Career Award from the Mathematical Biosciences Institute, Ohio State University (to Z.C.). K.T. and N.G.H. are with the University of Chicago, Chicago, IL 60637, USA. Z.C. is with the Massachusetts General Hospital/Harvard Medical School and MIT, Cambridge, MA 02139, USA. (Email: zhechen@mit.edu, kazutaka@uchicago.edu)

using standard cross-validation we employed the variational Bayes (VB) inference method in combination with automatic relevance determination (ARD) [10], [11]. The basic idea is to employ a closed-form sparse Bayesian learning framework to prune irrelevant input features. The hierarchical VB-ARD framework also allows us to impose conjugate priors to derive analytic solutions.

We have tested three models (all employed by sparse Bayesian methods): a static linear model, a linear dynamic (state-space) model, and a nonlinear dynamic model (while gradually increasing model complexity). In all experiments, we used 70% of the data for inferring the model (encoding), and used the remaining 30% of the data for decoding.

2) Static linear regression (LR) model: The standard decoding method is a linear Gaussian model that directly relates the input of neuronal firing rates (represented by a vector $\mathbf{u} \in \mathbb{R}^m$, here m=440) to the decoded output of interest $\mathbf{z} \in \mathbb{R}^n$ (where n denotes the dimensionality of kinematics), which can be either Cartesian kinematic variables or joint angles

$$\mathbf{z}_k = \mathbf{D}\mathbf{u}_k + \mathbf{v}_k \tag{1}$$

where k denotes the discrete time index, $\mathbf{D}$ denotes a time-invariant spatial filter (with independent row vectors $\{\mathbf{D}_i\} \in \mathbb{R}^m$), and $\mathbf{v}$ denotes a zero mean Gaussian noise variable. Instead of using the standard Wiener solution from linear regression, we employed a VB solution by assuming the following probabilistic model

$$p(\mathbf{z}|\mathbf{u}, \mathbf{D}, \tau) = \prod_{i=1}^{n} p(z_i|\mathbf{D}_i\mathbf{u}, \tau) = \prod_{i=1}^{n} \mathcal{N}(\mathbf{D}_i\mathbf{u}; \tau^{-1}) \tag{2}$$

$$p(\mathbf{D}_i, \tau|\boldsymbol{\alpha}) = \mathcal{N}(0; \tau^{-1} diag\{\alpha_1, \ldots, \alpha_m\}) \texttt{Gamma}(\tau|a_0, b_0) \tag{3}$$

$$p(\alpha_j) = \texttt{Gamma}(c_0, d_0) \;\; (j = 1, \ldots, m) \tag{4}$$

where τ denotes the precision parameter (inverse of variance) of the Gaussian; $\boldsymbol{\alpha} = \{\alpha_j\}_{j=1}^m$ and (a_0, b_0) denote the hyperparameters for the Gaussian and gamma distributions, respectively; and (c_0, d_0) are the hyperprior parameters. Upon completing VB-ARD inference in encoding, we obtained the variational posterior $q(\mathbf{D})$, which was subsequently used for decoding.

3) State space model (SSM): State space models with various formulations have been widely used in neural encoding/decoding (e.g., [12], [4]). Specifically, it is assumed that at each time step k, the hidden state $\mathbf{x}_k \in \mathbb{R}^N$ is driven by the previous state and a vector of firing rates $\mathbf{u}_k$ from N_c units

$$\mathbf{x}_k = \mathbf{A}\mathbf{x}_{k-1} + \mathbf{B}\mathbf{u}_k + \mathbf{w}_k \tag{5}$$

$$\mathbf{z}_k = \mathbf{C}\mathbf{x}_k + \mathbf{D}\mathbf{u}_k + \mathbf{v}_k \tag{6}$$

where $\mathbf{A}$ describes the state evolution; $\mathbf{B}$ and $\mathbf{C}$ represent the influence of firing rates $\mathbf{u}$ on the state and output, respectively; $\mathbf{z}$ denotes the predicted (Cartesian kinematics or joint angle) output; $\mathbf{w}$ and $\mathbf{v}$ represent zero-mean Gaussian noise in the state and measurement equations, respectively. The size of the hidden state vectors was inferred using the VB-ARD framework, with the maximum order of 5 (so as to reduce the computational complexity). The encoding model was estimated from a VB-EM algorithm [10]. The matrix $\mathbf{D}$ was initialized from the solution of Eq. (1). In the decoding phase, $\mathbf{x}_0 = 0$ was fed into the dynamic model to iteratively compute the output (without the need of running a Kalman filter).

4) Nonlinear Echo state network (ESN): The echo state network (ESN) is a recurrent neural network with a large, random fixed "reservoir" based on reservoir computing [13]. The hidden echo state $\mathbf{x} \in \mathbb{R}^N$ (typically N is very large) follows a state-space nonlinear system equation

$$\mathbf{x}_k = f(\mathbf{W}\mathbf{x}_{k-1} + \mathbf{W}^{in}\mathbf{u}_k + \mathbf{W}^{fb}\mathbf{z}_k) \tag{7}$$

$$\mathbf{z}_k = \mathbf{W}^{out}[\mathbf{x}_k; \mathbf{u}_k] \tag{8}$$

where f is a logistic sigmoid function, $\mathbf{W}$, $\mathbf{W}^{in}$ and $\mathbf{W}^{fb}$ are fixed and random weight matrices with proper dimensions for echo states, input, and feedback output, respectively. These matrices were randomly initialized within $[-a, a]$ (uniformly) with sparsity of 1% connectivity. The scale parameter a was set to 1 and the spectral radius of $\mathbf{W}$ was set to 0.8. The output weight matrix $\mathbf{W}^{out}$ was inferred in a similar way as in the LR model.

III. Results

A. Result Assessment

For decoding assessment, we used (i) the Pearson's correlation (between the predicted and actual variables), (ii) the mean absolute error (MAE), and (iii) the normalized MAE (NMAE) for individual output (scalar) variables

$$NMAE(z) = \frac{\text{mean}\{|z_k - \hat{z}_k|\}_k}{\text{standard dev}\{z\}}. \tag{9}$$

Since NMAE is normalized by the SD of the output z, it is dimensionless and invariant to the scaling of z. To assess the importance of individual units in decoding, we computed the importance index (II) for every unit by using a leave-one-out (loo) decoding strategy: we used all units during the encoding phase and decoded the output by either using all units or leaving one unit out (i.e., setting that unit's input as zero). The II for the c-th unit is defined as

$$II_c(z) = \frac{MAE_{loo}(z) - MAE(z)}{MAE(z)} \tag{10}$$

where MAE_{loo} denotes the new MAE by leaving the c-th unit out. A positive value of $II_c(z)$ implies that $MAE_{loo} > MAE$ for decoding the variable z, while a negative value of $II_c(z)$ implies that the inclusion of the c-th unit actually hurts the decoding performance. From $\{II_c\}_{c=1}^{N_c}$, we further computed the II-ratio by counting the total number of positive II_c normalized by N_c.

Furthermore, we assessed the prediction accuracy by computing the area under the receiver operative characteristic curve (AUC) (see [2] for the method) on the test data by using a trajectory-based encoding model (without the spike history) similar to [1].

B. Comparison of models

1) Object-specific decoding: We applied three models described in the Method section on the same test data. We first evaluated the decoding results separately for different objects. In total, we decoded 27 joint angles and six 3D Cartesian kinematic variables (position plus velocity, where $\{x, y, z\}$ represent the wrist position in the up-down, left-right, and forward-backward directions). Overall, the performance of Pearson's correlation from the three models was comparable (no significant difference); but the sparse LR model had the overall lowest NMAE (especially in joint angles). In addition, the decoding accuracy varied across different Cartesian kinematic variables and joint angles and different across objects. The correlation between the actual and decoded variables varied between -0.30 and 0.97. Figure 2 presents an illustration of good decoding results using a sparse LR model. Notably, decoding accuracy is much better for the y and z coordinates than the x coordinate (for both position and velocity). The comparison of Pearson's correlation among the three methods is shown in Fig. 3 and Fig. 4, for position/velocity kinematics and six selected joint

TABLE I

Summary of NMAE performance of three methods on the wrist Cartesian position/velocity and selected joint angles. Mean±SEM were computed across objects. Bold font indicates the best average performance. The first 4 joint angles are proximal and the remaining 12 angles are distal.

	sparse LR	sparse SSM	sparse ESN
x-position	$\mathbf{0.604 \pm 0.039}$	0.659 ± 0.041	0.606 ± 0.038
y-position	0.267 ± 0.004	0.270 ± 0.023	$\mathbf{0.261 \pm 0.005}$
z-position	0.230 ± 0.009	0.225 ± 0.018	$\mathbf{0.227 \pm 0.009}$
x-velocity	$\mathbf{0.514 \pm 0.036}$	0.542 ± 0.046	0.579 ± 0.091
y-velocity	$\mathbf{0.267 \pm 0.007}$	0.299 ± 0.016	0.315 ± 0.048
z-velocity	$\mathbf{0.256 \pm 0.007}$	0.263 ± 0.011	0.318 ± 0.062
elv angle	$\mathbf{1.254 \pm 1.018}$	1.555 ± 1.275	2.227 ± 1.972
shoulder elv	$\mathbf{0.422 \pm 0.033}$	0.475 ± 0.044	0.554 ± 0.048
shoulder rot	$\mathbf{0.529 \pm 0.046}$	0.645 ± 0.041	0.781 ± 0.082
elbow flexion	$\mathbf{1.251 \pm 0.882}$	1.552 ± 1.168	2.203 ± 1.708
pro sup	$\mathbf{0.560 \pm 0.083}$	0.705 ± 0.138	0.709 ± 0.109
wrist deviation	$\mathbf{0.485 \pm 0.084}$	0.620 ± 0.156	0.593 ± 0.120
wrist flexion	$\mathbf{1.202 \pm 0.722}$	1.871 ± 1.224	2.156 ± 1.577
cmc flexion	$\mathbf{0.707 \pm 0.181}$	0.822 ± 0.242	1.082 ± 0.387
cmc abduction	$\mathbf{0.826 \pm 0.310}$	0.985 ± 0.436	1.346 ± 0.699
mp flexion	$\mathbf{0.723 \pm 0.107}$	0.970 ± 0.169	0.929 ± 0.208
ip flexion	$\mathbf{4.560 \pm 4.005}$	6.907 ± 6.249	7.794 ± 7.144
2mcp flexion	$\mathbf{0.873 \pm 0.366}$	1.410 ± 0.793	1.243 ± 0.616
2mcp abduction	$\mathbf{0.614 \pm 0.095}$	0.745 ± 0.119	0.739 ± 0.120
2mp flexion	$\mathbf{2.966 \pm 2.380}$	4.660 ± 3.841	4.889 ± 4.108
2md flexion	$\mathbf{0.568 \pm 0.118}$	1.135 ± 0.501	0.782 ± 0.187
3mcp flexion	$\mathbf{0.717 \pm 0.252}$	1.837 ± 0.832	1.148 ± 0.519

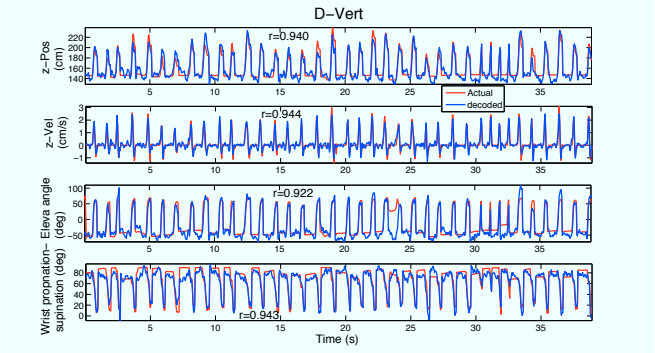

Fig. 2. An illustration of decoding 3D reach and grasp movement to the vertical D-ring. Pearson's correlation r is shown in each panel. In this example, the sparse Bayesian LR model was used, the MAE for these four variables are 5.54 cm, 0.16 cm/s, 10.23 deg and 5.90 deg, respectively.

angles, respectively. Surprisingly, the simplest sparse Bayesian LR model achieved relatively robust results. This was partially due to the fact that we used a sparse Bayesian inference method: if we instead employed a least-squares (non-sparse) solution for the LR model, the decoding performance degraded significantly (result not shown). Table I summarizes the NMAE results.

2) All-object decoding: Next, we tested the generalization of the three decoders across all objects. To do this, we combined all trials across all objects and repeated the encoding/decoding analysis (70% training and 30% testing data). The results on the Pearson's correlation are summarized in Table II. As seen, the ESN achieved the best decoding performance (highest correlation) for position and velocity; while the sparse Bayesian LR model achieved the best decoding performance for nearly all joint angles (correlation varied from 0.11 to 0.87). For this reason, we used the simplest yet robust sparse Bayesian LR model for the subsequent analysis.

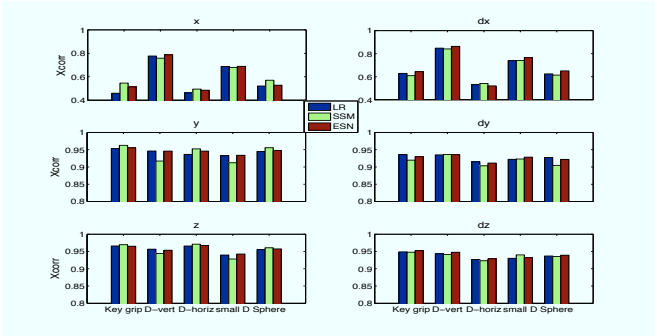

Fig. 3. Comparison of Pearson's correlation for the wrist Cartesian position (x, y, z) and velocity (dx, dy, dz) across objects from the three models.

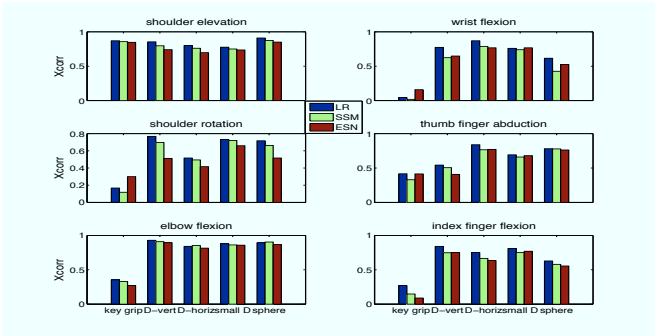

Fig. 4. Comparison of Pearson's correlation for six selected joint angles (left: proximal; right: distal) across objects from the three models.

C. Sensitivity of M1 Units for Decoding

To assess the contribution of individual M1 units to decoding, we computed the II (Eq. 10) and the II-ratio. A large positive II indicates that the unit is important for decoding. See Fig. 5 for an illustration. Based on this criterion, we can sort the units by their importance indices and assess their encoding properties, such as the AUC (Fig. 5 bottom panel). Depending on the decoded variable, the II-ratio varied between 0.36 and 0.86.

D. Joint Angles: Proximal vs. Distal Representations

Recording from a rigid electrode array during unconstrained 3D reach-to-grasp provides an opportunity to examine the potential spatial organization of proximal and distal movement representations across the precentral gyrus. Physiological studies based on intracortical microstimulation (ICMS) [14] have suggested a topographic organization across the precentral gyrus such that

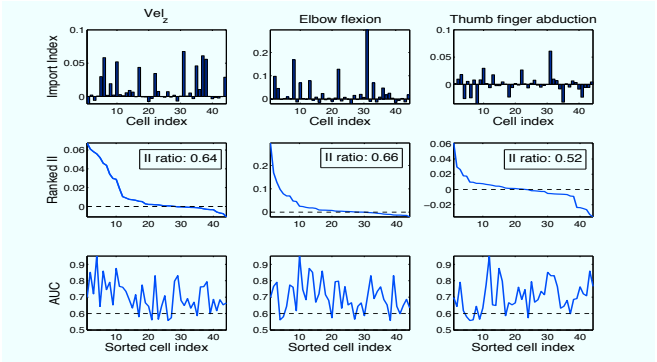

Fig. 5. Importance indices of all 44 units (1st row) and II-ratio (2nd row) in decoding and their respective AUC statistics (3rd row) in encoding. The x-axes of the 2nd and 3rd rows are the sorted version of the 1st row.

TABLE II

Summary of Pearson's correlation of three methods in all-object decoding. Bold font indicates the best performance.

	sparse LR	sparse SSM	sparse ESN
x-position	0.617	0.566	**0.644**
y-position	0.943	0.935	**0.949**
z-position	0.952	0.953	**0.958**
x-velocity	0.712	0.711	**0.733**
y-velocity	0.920	0.916	**0.924**
z-velocity	0.932	0.930	**0.940**
elv angle	**0.869**	0.784	0.853
shoulder elv	**0.823**	0.746	0.735
shoulder rot	**0.458**	0.233	0.366
elbow flexion	**0.819**	0.711	0.771
pro sup	**0.736**	0.659	0.691
wrist deviation	0.753	**0.790**	0.694
wrist flexion	**0.681**	0.500	0.563
cmc flexion	**0.578**	0.431	0.482
cmc abduction	**0.632**	0.475	0.580
mp flexion	**0.582**	0.335	0.454
ip flexion	**0.463**	0.312	0.328
2mcp flexion	**0.636**	0.414	0.535
2mcp abduction	**0.643**	0.604	0.616
2mp flexion	**0.543**	0.309	0.374
2md flexion	**0.110**	0.043	0.093
3mcp flexion	**0.159**	0.104	0.112

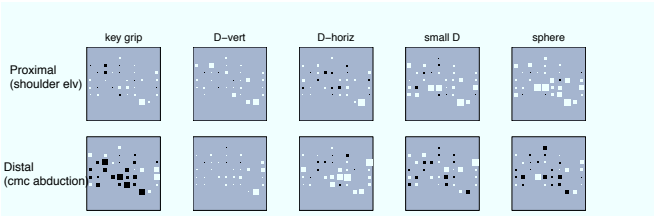

Fig. 6. Object-specific Hinton diagrams of mapping population units' importance indices onto the microelectrode array (the central sulcus is about 20-30 deg counterclockwise along the x-axis, array orientation is shown in Fig. 7). For illustration purpose, one proximal (shoulder elevation) and one distal (thumb finger abduction) joint angles are shown. The size of the square is proportional to the cumulative sum of importance indices at each channel. White/black color represents the net positive/negative value.

proximal movements of the shoulder and elbow are more often elicited rostrally whereas distal movements of the wrist and fingers are usually elicited caudally near the central sulcus. A population decoding approach provides a way to explore this issue. In our decoding analysis, the decoding accuracy of joint angles from the shoulder and elbow (proximal) varied across objects (Fig. 4), with the best performance for the "vertical D-ring" and "sphere" and poor performance for the "key grip" object. In contrast, the decoding accuracy of wrist and finger (distal) representation was highest for the "horizontal D-ring" and lowest for the "key grip" (Table I).

Figure 6 presents examples of Hinton diagrams of mapping 44 population units' importance indices onto the 10-by-10 array. As seen, the spatial patterns of proximal and distal representations varied with different object-grasping movements. The spatial patterns

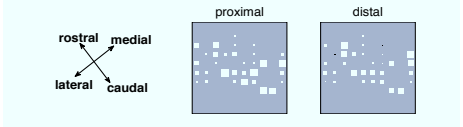

Fig. 7. Hinton diagrams of mapping population units' importance indices onto the microelectrode array in the case of all-objects decoding (with the same notation). The II of all units were computed based on the mean statistics of 4 proximal (center) and 8 distal (right) joint angles, respectively. Figures 6 and 7 share the same array orientation.

of M1 ensembles derived from our decoding analysis may provide insights into M1 population codes for object-specific reach to grasp movement. The analysis can be similarly applied to decoding all objects at all locations (Fig. 7). Based on our index of importance analysis, we did not observe a strong segregation between proximal and distal representations across the array.

IV. Summary

We have applied sparse Bayesian (VB-ARD) inference methods to decode 3D reach to grasp movements based on M1 neuronal ensembles. The simple sparse LR model achieved the overall best performance across objects and target locations. Based on the decoding analysis, we assessed the sensitivity of individual M1 units and evaluated the relative decoding performance of proximal and distal kinematic variables. Our results suggest that the M1 ensembles recorded from the precentral gyrus carried more proximal than distal information and yet there was significant information of distal joint angles from our recording site. It would be interesting to investigate how single cell representations as well as the network topology of the neuronal ensemble change dynamically during such unconstrained 3D reach to grasp movements. Future work will also examine object/location-invariant representations of M1 neuronal ensembles [15] during reach to grasp movements.

References

[1] N. G. Hatsopoulos, Q. Xu, Y. Amit, "Encoding of movement fragments in the motor cortex," *J. Neurosci.*, vol. 27, pp. 5105–5114, 2007.

[2] M. Saleh, K. Takahashi, and N. G. Hatsopoulos, "Encoding of coordinated reach and grasp trajectories in primary motor cortex," *J. Neurosci.*, vol. 32, pp. 1220–1332, 2012.

[3] A. L. Jacobs, *et al.*, "Ruling out and ruling in neural codes," *Proc. Natl. Acad. Sci. USA*, vol. 106, pp. 5936–5941, 2009.

[4] C. E. Vargas-Irwin, G. Shakhnarovich, P. Yadollahpour, J. M. K. Mislow, M. J. Black, and J. P. Donoghue, "Decoding complete reach and grasp actions from local primary motor cortex populations," *J. Neurosci.*, vol. 30, pp. 9659–9669, 2010.

[5] J. Zhuang, W. Truccolo, C. E. Vargas-Irwin, and J. P. Donoghue, "Decoding 3-D reach and grasp kinematics from high-frequency local field potentials in primary motor cortex," *IEEE Trans. Biomed. Eng.*, vol. 57, pp. 1774–1784, 2010.

[6] A. K. Bansal, W. Truccolo, C. E. Vargas-Irwin, and J. P. Donoghue, "Decoding 3D reach and grasp from hybrid signals in motor and premotor cortices: spikes, multiunit activity, and local field potentials," *J. Neurophysiol.*, vol. 107, pp. 1337–1355, 2012.

[7] H. A. Agashe, J. L. Contreras-Vidal, "Reconstructing hand kinematics during reach to grasp movements from electroencephalographic signals," in *Proc. EMBC'11*, pp. 5444–5447, 2011.

[8] X. Kang, M. H. Schieber, and N. V. Thakor, "Decoding of finger, hand and arm kinematics using switching linear dynamical systems with premotor cortical ensembles," in *Proc. EMBC'12*, pp. 1732–1735, 2012.

[9] V. Aggarwal *et al.*, "State-based decoding of hand and finger kinematics using neuronal ensemble and LFP activity during dexterous reach-and-grasp movements," *J. Neurophysiol.*, in press.

[10] M. J. Beal and Z. Ghahramani, "Variational Bayesian learning of directed graphical models with hidden variables," *Bayesian Analysis*, vol. 1, no. 4, pp. 793–832, 2006.

[11] K. P. Murphy, *Machine Learning: a Probabilistic Perspective*. Cambridge, MA: MIT Press.

[12] W. Wu, J. E. Kulkarni, N. G. Hatsopoulos, and L. Paninski, "Neural decoding of hand motion using a state-space model with hidden states," *IEEE Trans. NSRE*, vol. 17, no. 4, pp. 370–378, 2009.

[13] H. Jaeger, "Tutorial on training recurrent neural networks, covering BPPT, RTRL, EKF and the echo state network approach," GMD Report 159, Fraunhofer Institute AIS, 2002.

[14] M. C. Park *et al.*, "Consistent features in the forelimb representation of primary motor cortex in rhesus macaques," *J. Neurosci.*, vol. 21, no. 8, pp. 2784–2792, 2001.

[15] A. P. Georgopoulos, "Behavioral and neural aspects of motor topology: Following Bernsteins thread," *Progress in Motor Control, Volume 2: Structure-Function Relations in Voluntary Movements*, pp. 1–12, 2002.